Supplementary Information for

Patterns and driving mechanism of global marine phytoplankton blooms

Authors: Wei Hu[1,2], Jian-rong Ma[1,2,*], Hans W. Paerl[3], Erik Jeppesen[4,5,6,7,8], Justin D. Brookes[9], Jian Wu[10], Bo-qiang Qin[11,*]

Affiliations:

[1] Chongqing Institute of Green and Intelligent Technology, Chinese Academy of Sciences, Chongqing, China.

[2] Chongqing College, University of Chinese Academy of Sciences, Chongqing, China.

[3] Institute of Marine Sciences, Department of Earth, Marine and Environmental Sciences, UNC Chapel Hill, Morehead City, NC, USA.

[4] Department of Ecoscience, and WATEC, C.F. Møllers Allé 3, Aarhus University, Aarhus, Denmark.

[5] Sino-Danish Education and Research Centre, Beijing, China.

[6] Limnology Laboratory, Department of Biological Sciences and Centre for Ecosystem Research and Implementation, Middle East Technical University, Ankara, Turkey.

[7] Institute of Marine Sciences, Middle East Technical University, Mersin, Turkey.

[8] Institute for Ecological and Pollution Control of Plateau Lakes, School of Ecology and Environmental Science, Yunnan University, Kunming, China.

[9] School of Biological Sciences, University of Adelaide, North Terrace, Adelaide, Australia.

[10] Institute of Geographic Sciences and Natural Resources Research, Chinese Academy of Sciences, Beijing, China.

[11] Taihu Laboratory for Lake Ecosystem Research, State Key Laboratory of Lake Science and Environment, Nanjing Institute of Geography and Limnology, Chinese Academy of Sciences, Nanjing, China.

*Correspondence to: majianrong@cigit.ac.cn, qinbq@niglas.ac.cn

Supplementary Figures:

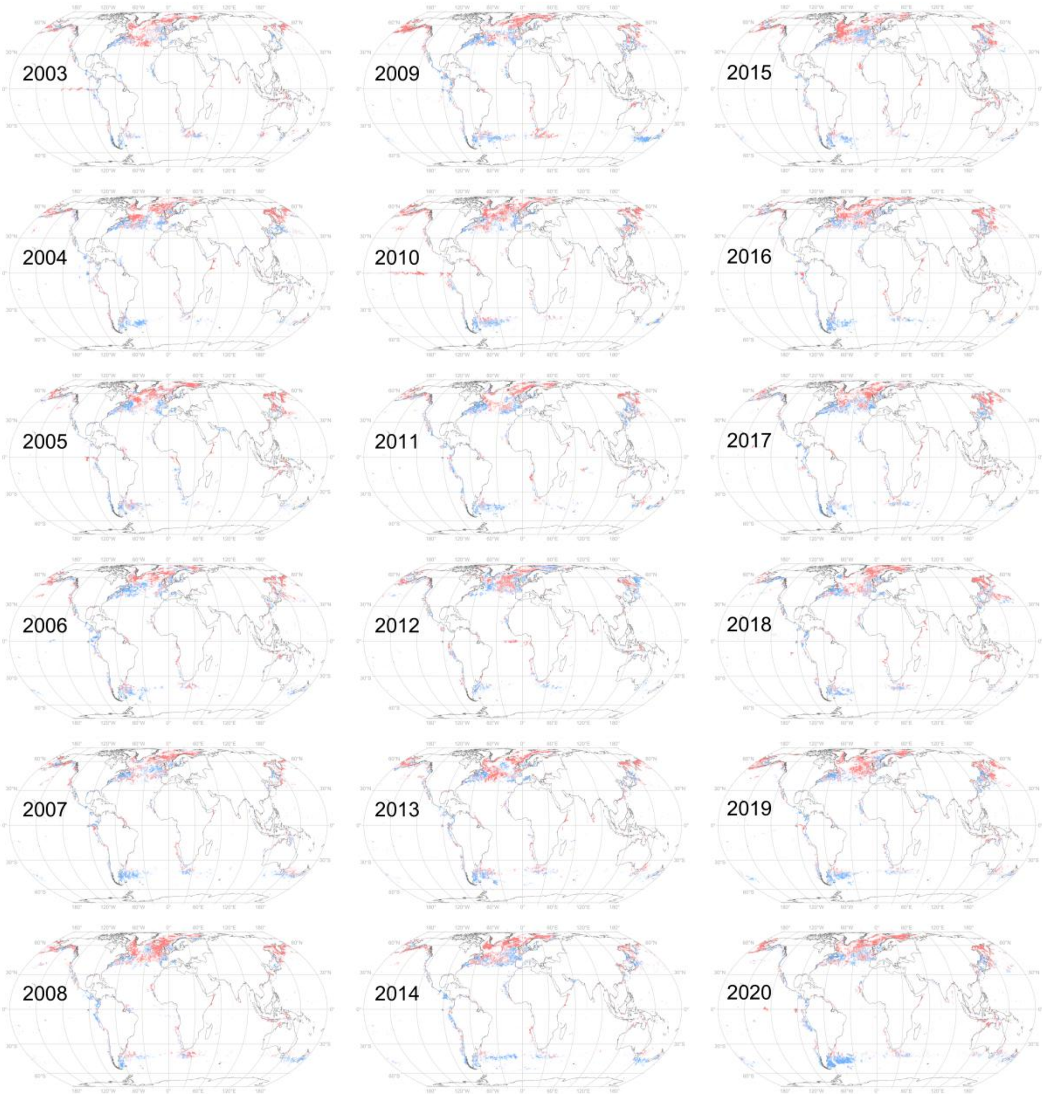

Supplementary Fig. 1 | Trend chart of the global marine algal bloom area during the 'first peak' from 2003 to 2020. The red regions indicate areas where new algal blooms emerged during the peak month compared to the previous month, while the blue regions indicate areas where algal blooms declined. The increase in algal blooms during the first peak month is primarily concentrated in the North Atlantic and North Pacific.

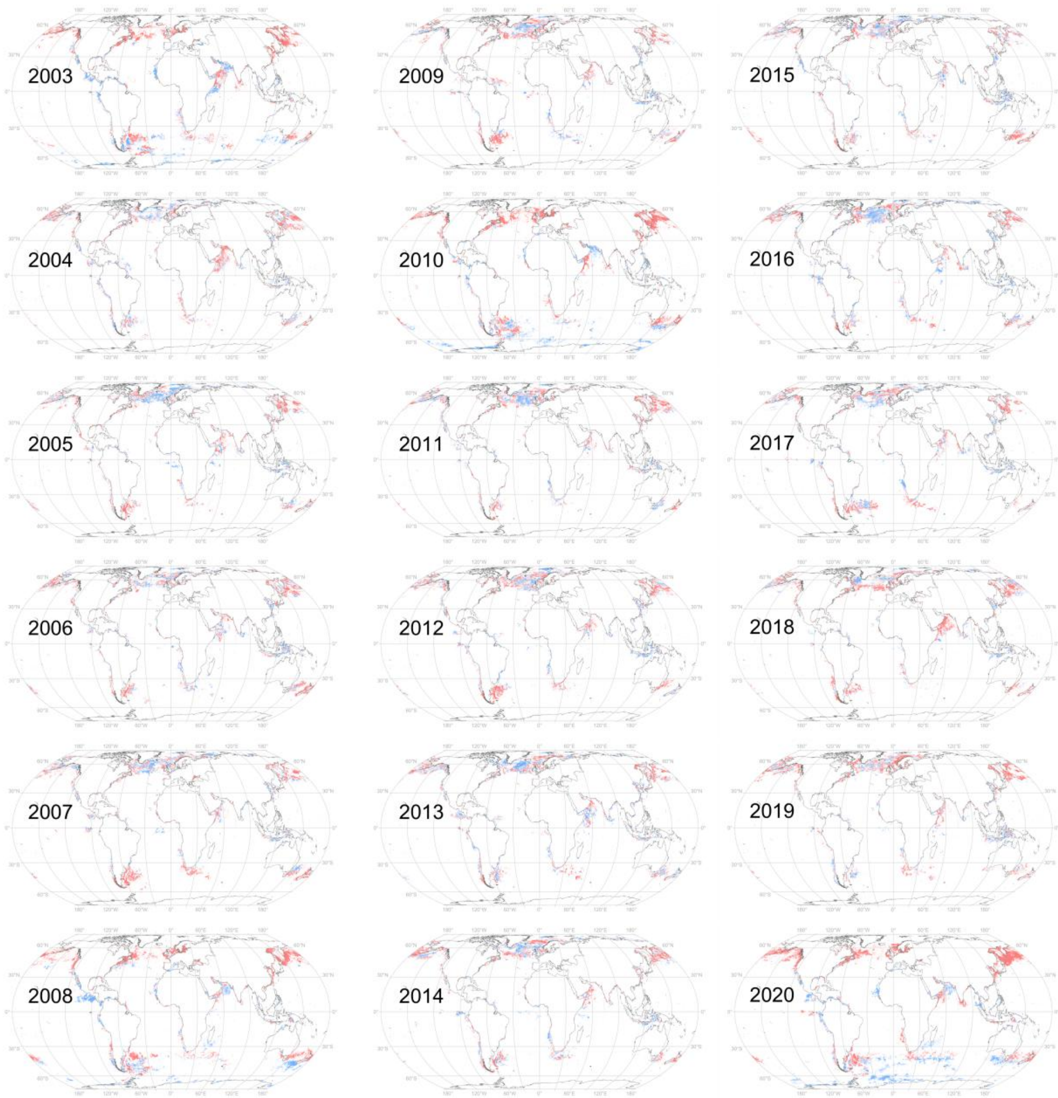

Supplementary Fig. 2 | Trend chart of the global marine algal bloom area during the 'second peak' from 2003 to 2020. The red regions indicate areas where new algal blooms emerged during the peak month compared to the previous month, while the blue regions indicate areas where algal blooms declined. The increase in algal blooms during the second peak month is primarily concentrated in the North Pacific.

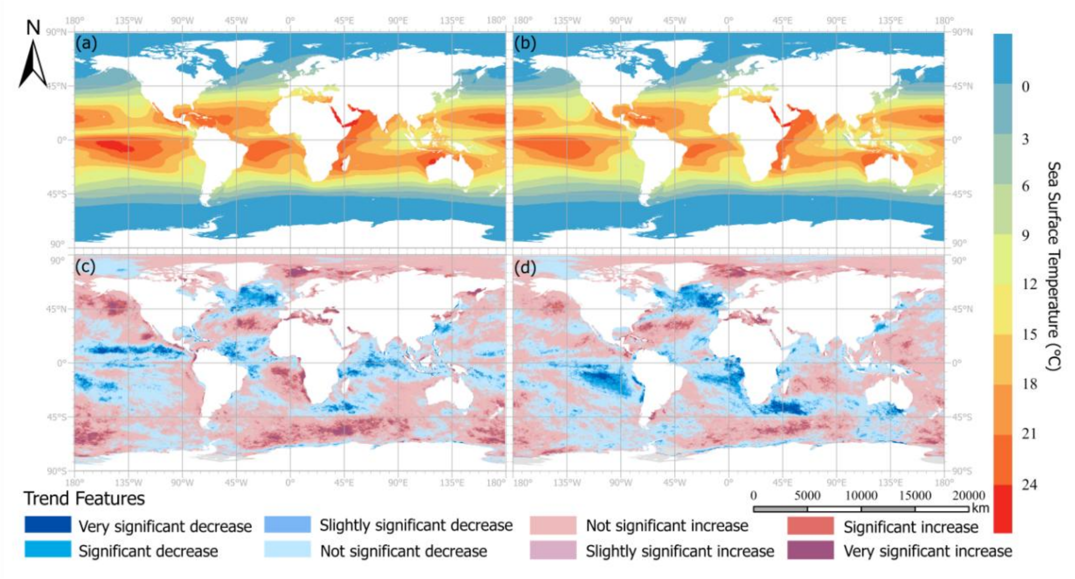

Supplementary Fig. 3 | Average annual SST and its changing trends from 2003 to 2020. The daytime temperature and its variation trend are depicted in **a** and **c**; the nighttime temperature and its variation trend are shown in **b** and **d**. The impact of wind and ocean currents prevents the temperature of the ocean's surface from displaying a latitude distribution. Certain open seas and certain coastal waters have warmer sea surface temperatures. The map was created using ArcGIS.

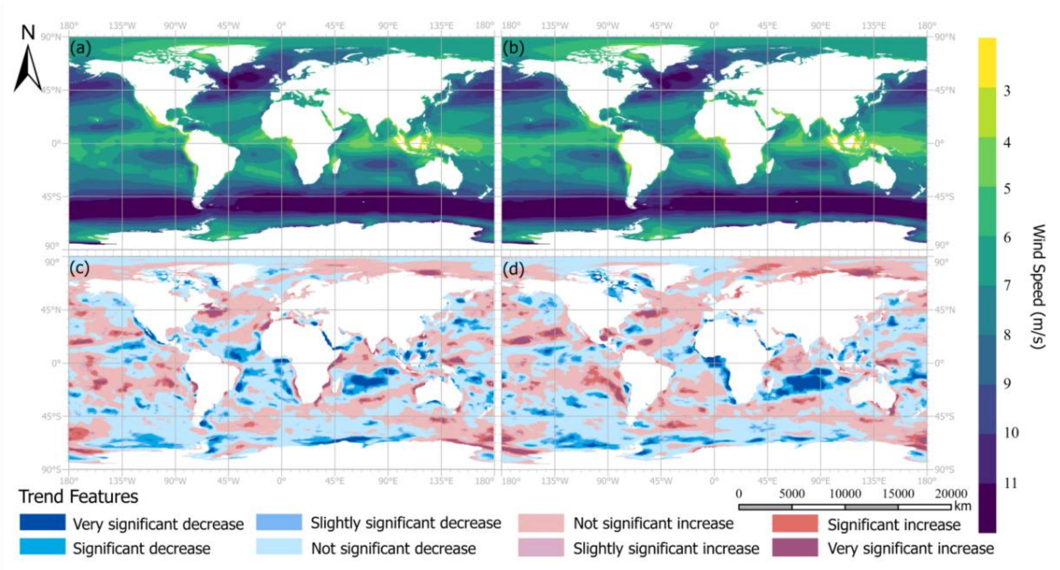

Supplementary Fig. 4 | Average annual wind speed and its changing trends from 2003 to 2020.

The daytime wind speed and its variation trend are depicted in **a** and **c**; the nighttime wind speed and its variation trend are shown in **b** and **d**. The westerly belt is the strongest wind zone in the world. The map was created using ArcGIS.

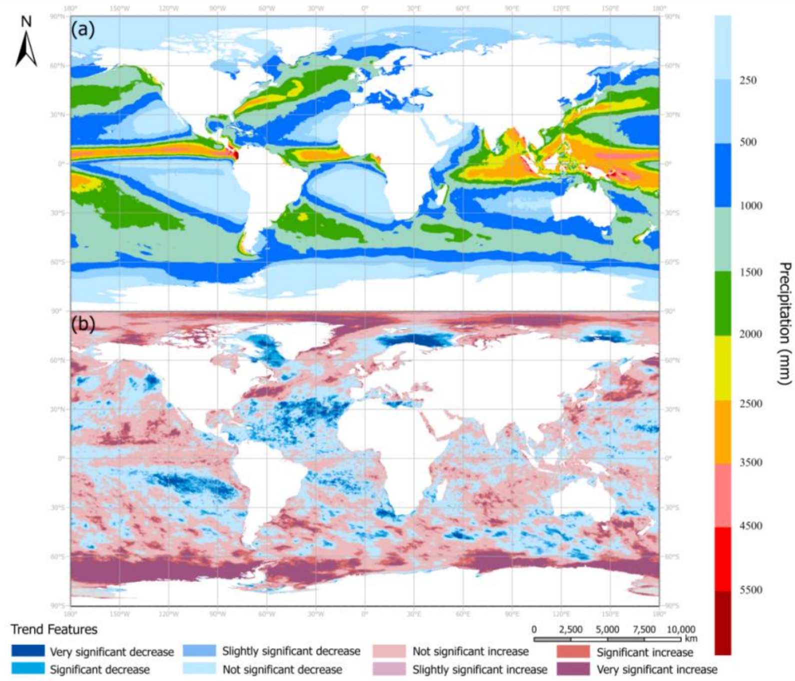

Supplementary Fig. 5 | Average annual total precipitation and its changing trends from 2003 to 2020. Average annual total precipitation depicted in **a.** Its variation trend are depicted in **b.** The equatorial rainbelt is the location of the global maximum rainfall, with comparatively large rainfall near the equator; similarly, the temperate rain belt experiences relatively large rainfall, with clear deviations attributed to monsoon influence. overall, the global rainfall trended upward during the study period. The map was created using ArcGIS.

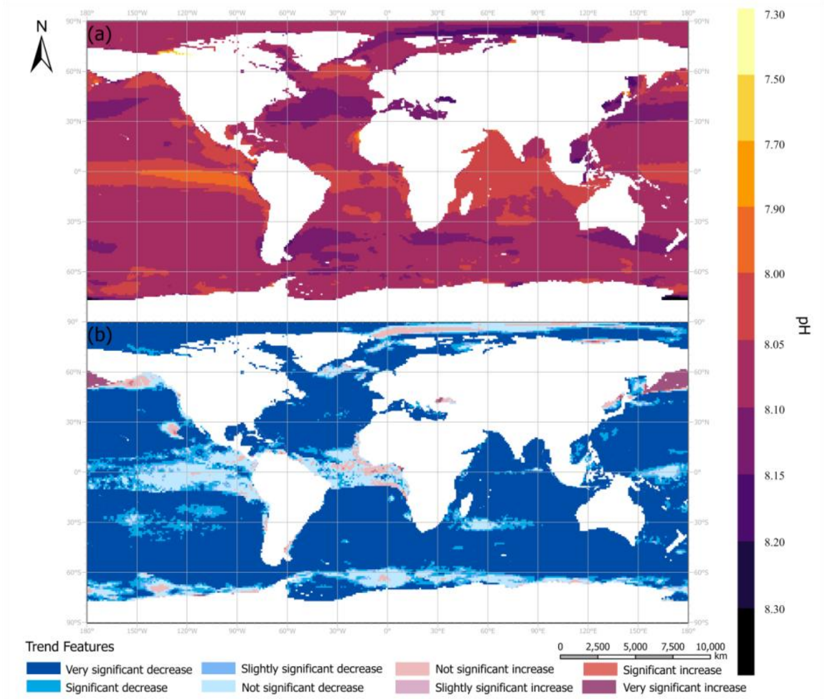

Supplementary Fig. 6 | Average annual pH and its changing trend of the sea surface (0 m) from 2003 to 2020. Average annual pH depicted in **a.** Its variation trend are depicted in **b.** Near the equator, the worldwide ocean pH value is lower; over the research period, the pH drastically drops and exhibits clear signs of acidification. The map was created using ArcGIS.

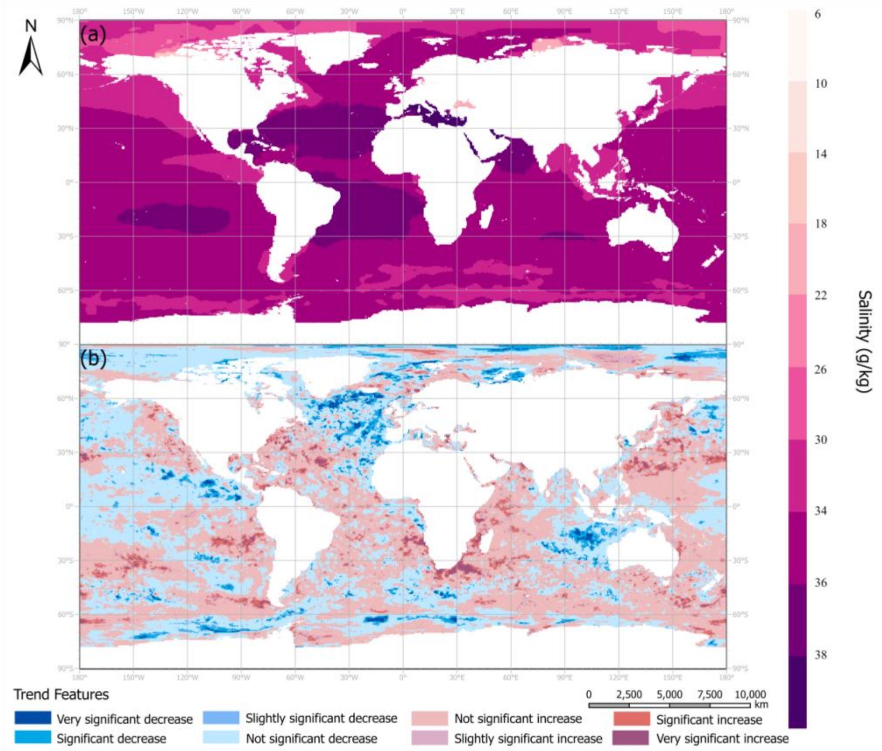

Supplementary Fig. 7 | Average annual salinity and its changing trend of the sea surface (0 m) from 2003 to 2020. Average annual salinity depicted in **a.** Its variation trend are depicted in **b.** Salinity is higher in the middle and low latitudes of Atlantic Ocean, and generally, salinity changes show an increasing trend. The map was created using ArcGIS.

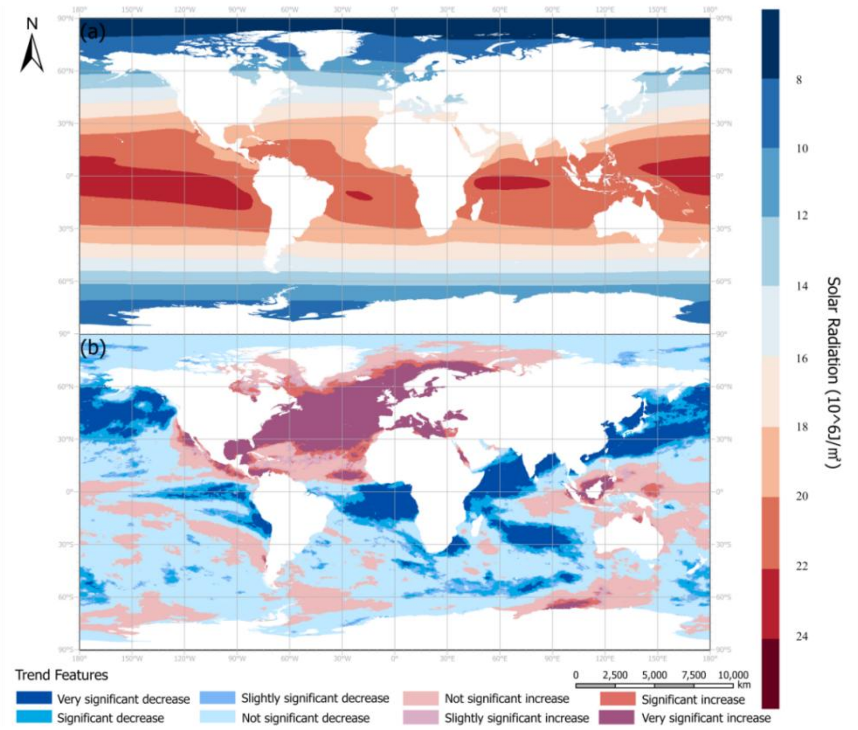

Supplementary Fig. 8 | Average annual solar radiation from 2003 to 2020 and its changing trend.

Average annual solar radiation depicted in **a.** Its variation trend are depicted in **b.** The yearly solar radiation distribution worldwide exhibits a very significant increase in the North Atlantic Ocean and a very significant decrease in the North Pacific Ocean, with latitude running parallel to the distribution. The map was created using ArcGIS.

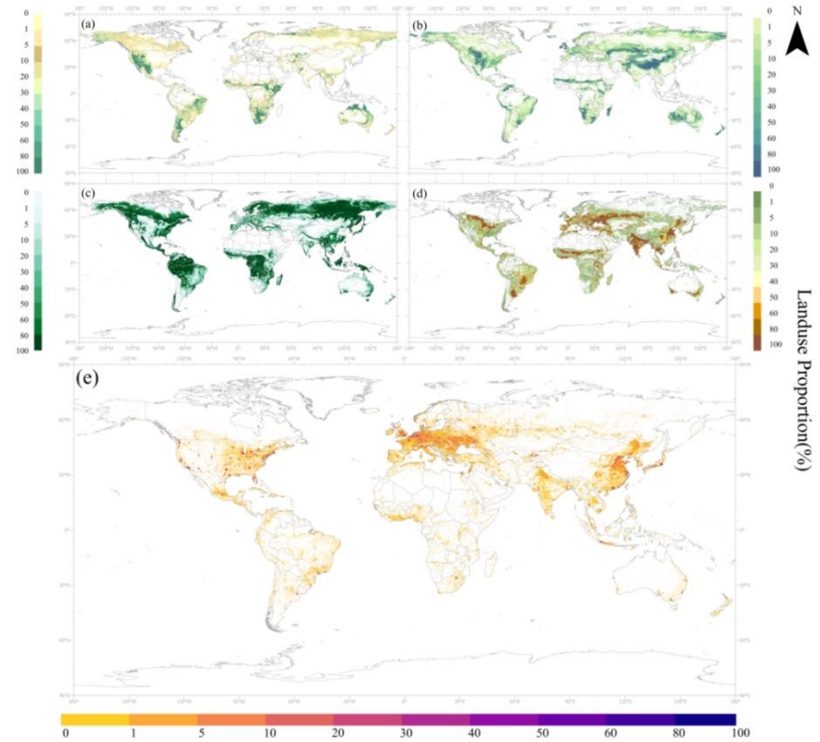

Supplementary Fig. 9 | Average annual proportion of different land use types from 2003 to 2020.

a, Shrub. **b,** Grass. **c,** Forest. **d,** Crop. **e,** Urban. The map was created using ArcGIS.

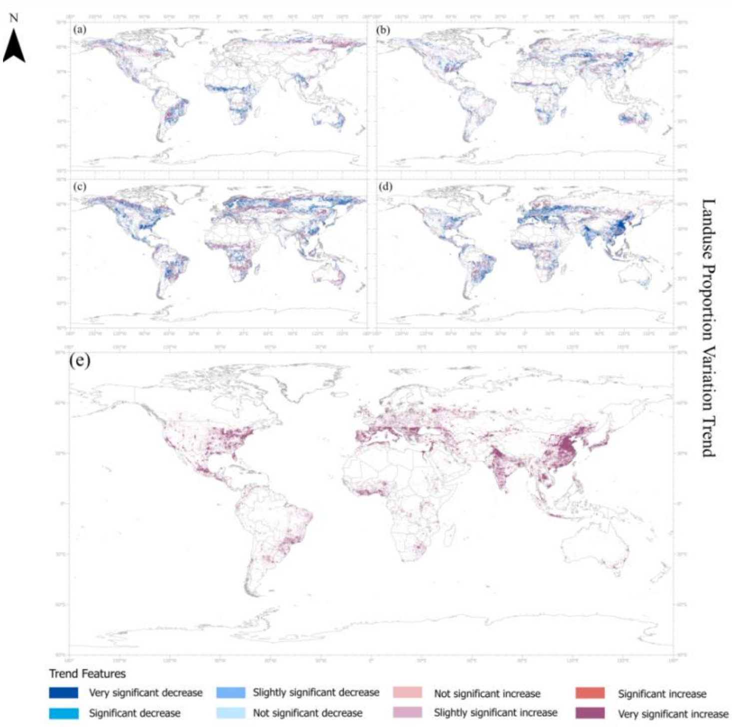

Supplementary Fig. 10 | Change trend of the average annual proportion of different land use types from 2003 to 2020. **a,** Shrub. **b,** Grass. **c,** Forest. **d,** Crop. **e,** Urban. The map was created using ArcGIS.

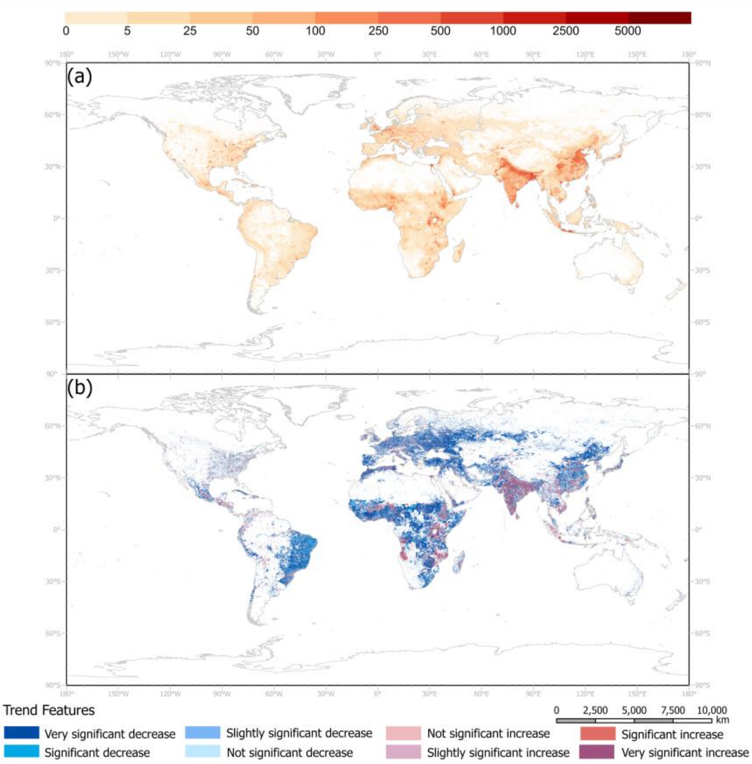

Supplementary Fig. 11 | Average annual Ambient Population from 2003 to 2020 and its changing trend. Average annual ambient population depicted in **a.** Its variation trend are depicted in **b.** The population is densely distributed in India, eastern and northern China, the central plains, and southwestern Indonesia. There are sporadic densely populated areas in other countries. At the same time, the population in most of these places has also shown an increasing trend. The map was created using ArcGIS.

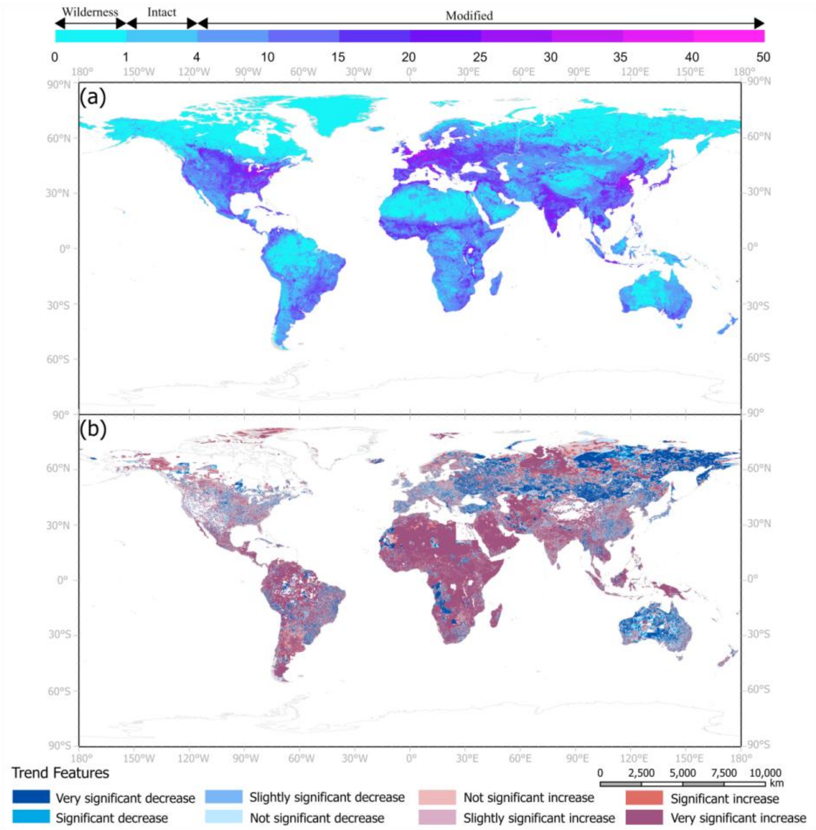

Supplementary Fig. 12 | Average annual Human Footprint Project from 2003 to 2020 and its changing trend. Average annual human footprint project depicted in **a**. Its variation trend are depicted in **b**. The footprints of human activities are higher in areas near coastal and inland waters, while in alpine and desert areas, the footprints of human activities are sparse. The map was created using ArcGIS.

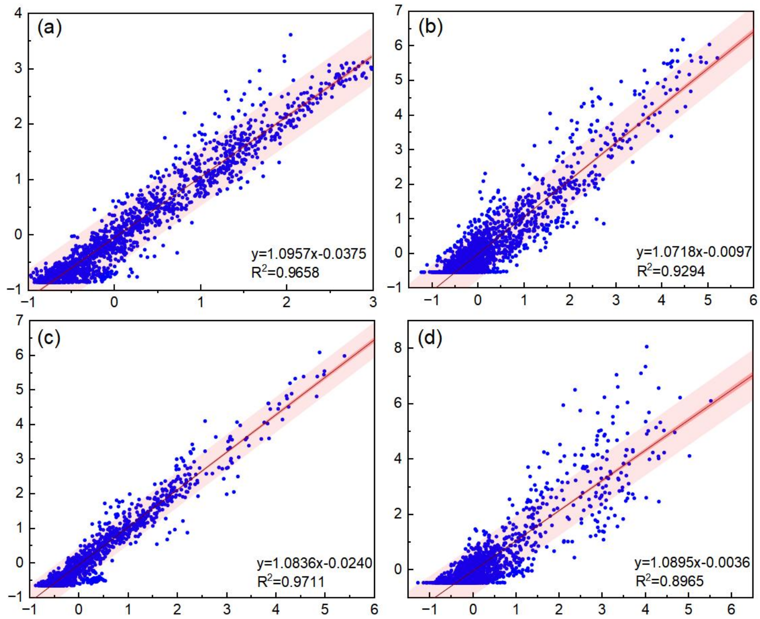

Supplementary Fig. 13 | Results of Linear Fitting of the GTWR Model's Predicted and Actual Values. The linear fitting results of GTWR model's predicted and actual values are presented for different regions and metrics of algal blooms: **a**, Model fitting results for the area affected by algal blooms in the coastal zone. **b**, Model fitting results for the area affected by algal blooms in open waters. **c**, Model fitting results for the cumulative number of days of algal blooms in the coastal zone. **d**, Model fitting results for the cumulative number of days of algal blooms in open waters. The map was created using Origin 2024.

Supplementary Tables:

Supplementary Tab. 1 The annual average of human footprint index and population count within 0.1 × 0.1 pixel in the Northern and Southern Hemispheres

Year	Human Footprint index		Population count	
	Northern Hemisphere	Southern Hemisphere	Northern Hemisphere	Southern Hemisphere
2003	6	2	78	34
2004	6	2	85	39
2005	6	2	93	41
2006	6	2	97	41
2007	6	2	98	41
2008	6	2	100	43
2009	7	2	102	44
2010	6	2	102	44
2011	6	2	104	50
2012	7	2	107	51
2013	7	2	109	51
2014	7	2	114	51
2015	7	2	118	53
2016	7	2	121	54
2017	7	2	128	57
2018	7	2	133	61
2019	7	2	142	64
2020	7	2	160	81

Supplementary Tab. 2 Moran’ I index test results

Year	Moran’ I		Z-score		P-value	
	BAA	CBD	BAA	CBD	BAA	CBD
2003	0.4596	0.3762	10.0240	8.3352	0.0000	0.0000
2004	0.4521	0.4041	9.8791	8.9570	0.0000	0.0000
2005	0.4973	0.4556	10.8698	10.0608	0.0000	0.0000
2006	0.4562	0.4534	9.9627	10.0483	0.0000	0.0000
2007	0.4918	0.4532	10.7610	9.9987	0.0000	0.0000
2008	0.4768	0.4980	10.4506	11.0553	0.0000	0.0000
2009	0.5104	0.5291	11.1435	11.7021	0.0000	0.0000
2010	0.5082	0.4760	11.1235	10.5097	0.0000	0.0000
2011	0.5124	0.4101	11.2194	9.0678	0.0000	0.0000
2012	0.5121	0.4489	11.2259	9.9359	0.0000	0.0000
2013	0.5240	0.4979	11.4646	10.9018	0.0000	0.0000
2014	0.5219	0.4374	11.4403	9.7043	0.0000	0.0000
2015	0.4944	0.4479	10.8187	9.8412	0.0000	0.0000
2016	0.5242	0.4707	11.5262	10.3535	0.0000	0.0000
2017	0.5175	0.4134	11.3722	9.1326	0.0000	0.0000
2018	0.5037	0.4666	10.9682	10.1877	0.0000	0.0000
2019	0.4933	0.4246	10.7570	9.3097	0.0000	0.0000
2020	0.4762	0.4661	10.4170	10.2247	0.0000	0.0000

Supplementary Tab. 3 Multicollinearity test results of BAA influencing factors in open water

	unstandardized coefficient		standardized coefficient			collinearity statistics	
	B	standard error	Beta	t	Significance	Tolerance	VIF
(constant)	-0.0410	0.0500		-0.8160	0.4150		
DSST	-0.1950	0.0330	-0.1880	-5.9360	0.0000	0.2900	3.4520
NWS	0.2970	0.0250	0.2880	12.0630	0.0000	0.5130	1.9500
PH	0.0500	0.0190	0.0480	2.5510	0.0110	0.8250	1.2120
PREC	0.2390	0.0210	0.2310	11.4480	0.0000	0.7180	1.3940
SA	0.3060	0.1540	0.0540	1.9910	0.0470	0.3910	2.5570

Dependent variable: BAA

Supplementary Tab. 4 Multicollinearity test results of BAA influencing factors in continental coastal waters

	unstandardized coefficient		standardized coefficient			collinearity statistics	
	B	standard error	Beta	t	Significance	Tolerance	VIF
(constant)	-0.3700	0.0790		-4.6730	0.0000		
DSST	-0.2890	0.0700	-0.2690	-4.1420	0.0000	0.1100	9.0940
NWS	0.3560	0.0370	0.3450	9.7060	0.0000	0.3670	2.7270
pH	-0.1550	0.0280	-0.1510	-5.4450	0.0000	0.6050	1.6530
Prec	0.0850	0.0270	0.0820	3.1910	0.0010	0.6990	1.4300
SR	0.0760	0.0560	0.0700	1.3530	0.1760	0.1710	5.8500
Sa	1.2220	0.1710	0.2590	7.1500	0.0000	0.3530	2.8300
Pop	0.0940	0.0360	0.0830	2.5900	0.0100	0.4550	2.1990
HFP	-0.0350	0.0310	-0.0330	-1.1190	0.2630	0.5400	1.8520
Urban	0.0140	0.0310	0.0130	0.4710	0.6380	0.6190	1.6160
Shurb	-0.0590	0.0290	-0.0550	-2.0370	0.0420	0.6400	1.5610
Grass	-0.1350	0.0320	-0.1080	-4.2160	0.0000	0.7000	1.4280
Forest	-0.0790	0.0300	-0.0700	-2.6460	0.0080	0.6710	1.4900
Crop	0.0560	0.0320	0.0480	1.7550	0.0790	0.6140	1.6280

Dependent variable: BAA

Supplementary Tab. 5 Multicollinearity test results of CBD influencing factors in open water

	unstandardized coefficient		standardized coefficient			collinearity statistics	
	B	standard error	Beta	t	Significance	Tolerance	VIF
(constant)	-0.3120	0.0510		-6.1540	0.0000		
pH	-0.0400	0.0210	-0.0390	-1.9350	0.0530	0.7870	1.2710
Prec	0.2800	0.0240	0.2700	11.718	0.0000	0.5890	1.6990
Sa	1.2930	0.1610	0.2290	8.0490	0.0000	0.3860	2.5920
SR	-0.5270	0.0350	-0.5130	-14.972	0.0000	0.2650	3.7700
DWS	0.1380	0.0210	0.1330	6.7240	0.0000	0.7950	1.2590
Dependent variable: CBD							

Supplementary Tab. 6 Multicollinearity test results of BAA influencing factors in continental coastal waters

	unstandardized coefficient		standardized coefficient			collinearity statistics	
	B	standard error	Beta	t	Significance	Tolerance	VIF
(constant)	-0.4010	0.0850		-4.6950	0.0000		
DSST	-0.5450	0.0750	-0.4800	-7.2720	0.0000	0.1110	9.0280
pH	-0.1570	0.0310	-0.1450	-5.1230	0.0000	0.6040	1.6540
Prec	-0.0940	0.0290	-0.0850	-3.2480	0.0010	0.6970	1.4350
SR	0.2590	0.0610	0.2260	4.2670	0.0000	0.1710	5.8400
Sa	1.1890	0.1850	0.2380	6.4400	0.0000	0.3520	2.8400
Pop	0.1010	0.0390	0.0840	2.5850	0.0100	0.4540	2.2040
HFP	0.0380	0.0340	0.0340	1.1220	0.2620	0.5400	1.8530
Urban	-0.0240	0.0330	-0.0200	-0.7170	0.4740	0.6200	1.6130
Shurb	-0.0050	0.0310	-0.0040	-0.1630	0.8710	0.6490	1.5400
Grass	-0.0270	0.0340	-0.0200	-0.7760	0.4380	0.7040	1.4210
Forest	-0.0650	0.0320	-0.0540	-2.0220	0.0430	0.6700	1.4920
Crop	0.0610	0.0340	0.0500	1.7770	0.0760	0.6170	1.6200
DWS	0.3340	0.0400	0.3010	8.3750	0.0000	0.3720	2.6860

Dependent variable: CBD

Supplementary Tab. 7 Related parameters of GTWR model results

	BAA		CBD	
	Coast water	Open water	Coast water	Open water
Bandwidth	49.2254	56.2623	49.2254	56.2623
Residual Squares	124.8067	415.3834	117.4729	603.2072
Sigma	0.2801	0.3876	0.2717	0.4671
AICc	467.4107	2607.4145	371.0622	3638.9218
R^2	0.7769	0.7520	0.8032	0.6770
Adjusted R^2	0.7750	0.7516	0.8015	0.6764
Spatio-temporal Distance Ratio	3.0342	3.0342	3.0342	3.0342

Supplementary discussion:

The changing trend of environmental factors

With respect to the worldwide distribution of ocean surface temperatures (Supplementary Fig. 3a and Supplementary Fig. 3b), the average daily temperature exceeds 24 ℃ in many regions, particularly along the coasts of the Middle East, Somalia, northeastern Australia, Madagascar, and the central Atlantic and Pacific. This temperature range supports the development and reproduction of algae. The only regions with average nighttime temperatures above 24 ℃ are the Red Sea, Persian Gulf, and Gulf of Oman. All other regions have nighttime temperatures below this threshold. At latitudes above 50° north and south, both daily highs and overnight lows are essentially below freezing. The trend in ocean surface temperature clearly indicates global warming (Supplementary Fig. 3c, Supplementary Fig. 3d). Over half of the ocean's surface shows an increasing trend in mean annual daylight temperature, with notable exceptions being the Mediterranean Sea, the Gulf of Alaska, the central North Atlantic, the African coast of the South Atlantic, and the Arctic and Antarctic regions. The daily average annual temperature exhibits a significant downward trend in most equatorial regions, the northern Atlantic Ocean, most of the Indian Ocean, the coast of Southeast Asia, the coast of eastern China, the southeastern coast of the United States, and the northern coast of Latin America. In contrast to the annual average daytime temperature, the coastal regions of western Africa, southern Australia, and northern Latin America show a trend where a significant increase in daytime temperature shifts to a significant decrease in nighttime temperature, resulting in a larger diurnal temperature range.

The greatest values are found in the vicinity of the westerly belt, regardless of the time of day or night. High-value wind speed centers, with wind speeds above 11 m s^{-1}, simultaneously occur in the northern seas of Latin America, the coast of Peru, the central Pacific Ocean, and the central Indian Ocean. Conversely, low-value centers, with wind speeds less than 4 m s^{-1}, low value centers emerge in Southeast Asia, the western coast of South America, and the northwest coast of Latin America (Supplementary Fig. 4a, Supplementary Fig. 4b). The regions that exhibited rising and decreasing trends in wind speed variations across the research period are generally near one another, forming a dispersed block distribution pattern (Supplementary Fig. 4c, Supplementary Fig. 4d).

Throughout the research period, there was a notable decrease in daytime wind speed along the western coast of North America, the central Indian Ocean, the Arabian Gulf, most of the western African coastlines, and the northwest and southeast coasts of South America. Conversely, there was a significant increase in daytime wind speed on the east coast of North America, the northeast and southwest coasts of South America, the north and east coasts of Africa, the Bay of Bengal, the southern coast of Southeast Asia, and most of Oceania's coasts. Wind speed variations in the Pacific Ocean exhibit greater erratic behavior, with a downward trend in the northern hemisphere and an upward trend in the southern hemisphere. The nighttime wind speed trend generally aligns with the daytime trend; however, the decrease in nighttime wind speed is more pronounced than during the day. Additionally, there are regions where the daytime and nighttime wind speed trends are reversed. For instance, in the coastal region of southwest Africa, daytime wind speed is trending upward, while nighttime wind speed is trending downward. This pattern is also observed in the coastal regions of Peru and Chile in South America.

The geographical distribution map of precipitation (Supplementary Fig. 5a) shows that the equatorial rainy belt is the location of the peak annual precipitation, with a maximum of around 10712 mm yr^{-1}, and that this belt is shifting northward. The east coasts of temperate zone continents receive higher summer precipitation due to monsoons and warm currents, in addition to the comparatively high yearly rainfall near the equator. Consequently, these regions see annual precipitation exceeding 1,000 mm. In contrast, the west coasts of continents receive significantly less rainfall than that on the east coast due to the absence of such rainfall-promoting elements. Southeast Asia, regardless of the coastal orientation, receives between 1,500 and 2,000 mm of precipitation annually. The arctic regions and the subtropical regions along the continent's western coast are home to areas with minimal rainfall. During the research period, there was a noticeable upward trend in annual precipitation in the polar areas. However, a distinct 'Matthew effect' was observed, indicating an increasing trend in regions already experiencing high annual rainfall. Conversely, in smaller regions, annual rainfall trends showed polarization and a downward trend (Supplementary Fig. 5b).

The global ocean's pH ranges primarily between 7.90 and 8.15, with the majority falling between 8.05 and 8.10. In the coastal zones of Southeast Asia, the pH ranges from 8.10 to 8.20, while it decreases towards the equator, averaging between 7.90 and 8.05 (Supplementary Fig. 6a). Additionally, high pH values are observed in the Arctic seas, the Mediterranean Sea, the northern coast of East Asia, the southern coast of Africa, the east and west coasts of southern South America, the central North Pacific, and the central North Atlantic. A significant declining trend in pH is evident across most of the world's oceans, indicating a trend toward acidification. Only a very small portion of the marine regions show an increasing trend in pH values. For example, the western Gulf of Alaska and the Bering Sea exhibit a noticeable upward trend in pH values (Supplementary Fig. 6b).

Global ocean salinity predominantly ranges between 34-36g kg^{-1} (Supplementary Fig. 7a). The lowest average salinity value is 6.455g kg^{-1}, which occurs near the Baltic Sea, while the highest average salinity value is 40.82g kg^{-1}, which occurs near the Mediterranean Sea. The Red Sea and Persian Gulf also have higher salinity. In addition, within the range of 40°N-30°S in the Atlantic Ocean, the water salinity is basically 36-38g kg^{-1}. High salinity values are also present in parts of the Arabian Sea, the South Pacific, and the central regions of the South Indian Ocean. During the study period, only a small number of water bodies exhibited significant trends in salinity increase or decrease, with a relatively dispersed distribution. For instance, the North Atlantic waters near Europe showed a significant or highly significant decreasing trend, whereas the waters near the United States and Mexico exhibited a significant or highly significant increasing trend. Most of the global ocean salinity did not show significant changes over the study period. Notably, salinity in the Yellow Sea and the western Indian Ocean demonstrated significant or highly significant decreasing trends, while salinity in some waters west of South America and the coastal zones of southern Africa showed increasing trends (Supplementary Fig. 7b).

The distribution of solar radiation primarily follows latitudinal zones; however, in the tropics, solar radiation is higher in open waters, exceeding 24×10^6 J m^{-2}, and lower in waters close to the continental coast, primarily within the range of 22×10^6 J m^{-2} ~ 24×10^6 J m^{-2} (Supplementary Fig. 8a). The trend of solar radiation over the study period indicates that, while solar radiation over other sea areas, particularly above 30°N in the North Pacific, essentially showed a decreasing trend, solar radiation over the North Atlantic showed a significant (or extremely significant) increase. In general, there is a noticeable downward trend in solar radiation over and around the equator of the North Indian and South Atlantic Oceans. Moreover, the trend is essentially declining along the west coast of South America and increasing along the coast of Southeast Asia (Supplementary Fig. 8b).

East Asia, South Asia, and Southeast Asia have more forests and cultivated areas compared to shrub land. Regions with the highest concentrations of urban land include eastern China, Western Europe, and the east coast of the United States (Supplementary Fig. 9). During the research period, urban land use exhibited the most significant change, showing a substantial increasing trend globally (Supplementary Fig. 10e). Concurrently, there is a noticeable decline in cropland areas in China, India, and Europe (Supplementary Fig. 10d).

The population is densely concentrated in India, eastern and northern China, the central plains, and southwestern Indonesia, with sporadic densely populated areas in other countries (Supplementary Fig. 11a). It is also evident that a significant portion of the population resides near bodies of water. Generally, populations are concentrated in coastal, lake, and riverside locations. Notable examples include the African shore of the Nile River, particularly in the northern region near the Mediterranean Sea, and the population distribution around the Great Lakes in the United States. During the research period, there was a notable decrease in population density in regions such as eastern Brazil and northern Europe, and a significant increase in densely populated areas such as India (Supplementary Fig. 11b).

human footprint values are low in alpine and desert regions, such as the Sahara and areas between 60° N and 90° N. However, these values are higher near coastal and inland waters in eastern and southern Asia, western Europe, and eastern North America (Supplementary Fig. 12a). During the research period, the trend of human activity footprints exhibited a significant increase in most parts of the world, with only a notable decrease observed in eastern Russia and central and western Australia (Supplementary Fig. 12b).

Construction of Geographically and Temporally Weighted Regression

There is no significant collinearity among the explanatory variables since the GTWR model requires spatial autocorrelation of the explained events. The Moran's I index test confirms that BAA and CBD data exhibit spatial autocorrelation (Supplementary Tab. 2), aligning with the GTWR's requirement for "spatial autocorrelation of explained variables". The GTWR model, a linear model, necessitates that explanatory variable do not have severe collinearity (VIF < 10). The collinearity test results indicate high collinearity between solar radiation, daytime and nighttime wind speeds, and SST. Factors were screened by ranking the contribution rates of GeoDetector: in open water, the BAA driving mechanism excluded solar radiation, nighttime SST, and daytime wind speed; in coastal waters, the BAA driving mechanism excluded nighttime SST and daytime wind speed; in open water, the CBD driving mechanism excluded daytime SST, nighttime SST, and daytime wind speed; in coastal waters, the CBD driving mechanism excluded nighttime SST and nighttime wind speed. A multicollinearity test was performed on the screened variables, and the results are shown in Supplementary Tab. 3 to Supplementary Tab. 6.

The results indicate that the BAA-driven model for land coastal waters comprises daytime SST, nighttime wind speed, pH, rainfall, solar radiation, salinity, population, human footprint, and land use. For open waters, the BAA-driven model includes daytime SST, nighttime wind speed, pH, rainfall, and salinity. The CBD-driven model for land coastal waters consists of daytime SST, daytime wind speed, pH, rainfall, solar radiation, salinity, population, human footprint, and land use. The CBD-driven model for open waters includes rainfall, salinity, solar radiation, and daytime wind speed These models adhere to the GTWR requirement that "no strong collinearity exists in explanatory variables." All variables are independent and do not interfere with the model's stability due to mutual influence. Therefore, further modeling analysis is feasible.

Supplementary Tab. 7 displays the essential parameter results of the GTWR model used in this investigation. And Extended Data Fig. 9 shows the results of linear fitting of the GTWR Model's predicted and actual values. The R^2 values indicate that the model has a satisfactory fitting effect.

Major driving factors: A Spatiotemporal Regression Analysis

Temperature directly influences algal bloom development, but not all species of blooms have consistent temperature-growth responses globally[1]. In a majority of open seas, the regression coefficient between daytime SST and the BAA is positive, particularly in the North Atlantic and the Arabian Sea, indicating that rising temperatures have triggered blooms in these regions. Previous research has shown that the affected area of algal blooms increases with rising temperatures[1]. However, in coastal waters, the regression coefficient between daytime SST and BAA is negative (Extended Data Fig. 4a and Extended Data Fig. 4b), suggesting that higher sea surface temperatures result in smaller bloom sizes. Blooms typically appear after a certain temperature threshold is reached. When water temperatures rise beyond this threshold, the division rate of phytoplankton cells slows down or halts, eventually leading to the bloom's decline[2]. SST changes also have indirect effects on blooms, for instance, rising SST can increase ocean stratification, promoting the growth of *dinoflagellates*, which can migrate vertically to access deeper nutrients[3]. At high latitudes, stratification can isolate phytoplankton from nutrient-rich, colder upper waters[4], favoring *diatom* development over *dinoflagellates*[5]. Determining the precise net effect of SST on marine phytoplankton blooms is challenging due to the interaction between SST and other environmental factors, which often shows a significant two-factor amplification (Fig. 3b).

In general, wind speed has a beneficial impact on BAA (Extended Data Fig. 4c and Extended Data Fig. 4d), particularly in the North Atlantic and Arctic Ocean. This finding contrasts with the conventional wisdom that wind speed and algal blooms are inversely related[6]. However, the effect of wind on phytoplankton blooms largely depends on the wind's direction and the specific region it affects. Abnormally intense algal blooms can also occur during windy seasons[7]. For instance, westerly winds in the Southern Ocean carry aerosols laden with nutrients from Australian wildfires across the ocean, which are then deposited into the water by precipitation, leading to massive algal blooms[7]. Moreover, the annual average wind speed across most of the world's oceans is less than 8 $m*s^{-1}$, except in the westerly belt (Supplementary Fig. 4a and Supplementary Fig. 4b). This suggests that lower wind speeds do not submerge algae, causing the blooms to "disappear". Instead, they actively contribute to the migration and spread of the blooms. Consequently, there are regional variations in the effect of wind speed on marine phytoplankton blooms.

The impact of solar radiation on algal bloom dynamics varies significantly across different ocean regions. In coastal areas of North and South America, the North Pacific coast, and the Eastern Atlantic coast, solar radiation has a substantial positive effect on the BAA (Extended Data Fig. 4g and Extended Data Fig. 4h) and the CBD (Extended Data Fig. 5c and Extended Data Fig. 5d). Conversely, in open waters, solar radiation exhibits a slight negative effect on the cumulative number of algal bloom days (Extended Data Fig. 5c and Extended Data Fig. 5d). This phenomenon may be attributed to differences in water turbidity. Coastal areas often have turbid waters due to sediments such as silt carried by rivers, whereas open waters, far from land and human activities, are typically very clear. Water turbidity directly affects the penetration of solar radiation, thereby influencing light utilization by phytoplankton. Consequently, the impact of solar radiation differs markedly between coastal zones and open waters. Over time, the regression coefficients from 2003 to 2020 have remained relatively stable (Extended Data Fig. 5c and Extended Data Fig. 5d).

In 2003, salinity's influence on BAA was primarily observed in the coastal zones of Brazil and Argentina, the southern Atlantic Ocean, and the eastern sea area of Australia. Notably, the regression coefficient between BAA and salinity showed a positive effect only in New Zealand's coastal waters (Extended Data Fig. 4e). By 2020, salinity impacts on BAA had increased along the eastern coast of South America and near the equator in the western Pacific Ocean (Extended Data Fig. 4f). The effect of salinity on CBD is also more pronounced in coastal zones, particularly along the eastern coast of South America and the northeastern coast of Asia, exhibiting negative and positive effects, respectively (Extended Data Fig. 5a and Extended Data Fig. 5b). Over time, significant changes were observed in the North Pacific Ocean: salinity had a weak positive effect on bloom CBD in 2003 (Extended Data Fig. 5a) but a negative effect in 2020 (Extended Data Fig. 5b). Overall, salinity's negative impact on bloom dynamics is more significant in coastal zones, suggesting that intensified water circulation due to climate change[8] and large groundwater discharges[9] reduce coastal seawater salinity while enriching coastal ecosystems with nutrients, leading to increased blooms. For blooms more adaptive to high salinity environments (e.g., *Trichodesmium*[10]), the effect of salinity on bloom dynamics shows a positive impact in waters with high net evaporation and salinity.

The coastal zone of South Africa and the area near the North Pacific Ocean are regions where precipitation significantly impacts the CBD. These areas generally exhibit negative effects, while other sea areas show no readily apparent control effect (with regression coefficients between -2 and 2) (Extended Data Fig. 5e and Extended Data Fig. 5f). This indicates that periods of heavy precipitation limit phytoplankton biomass[11]. The strength of precipitation largely determines its impact on algal blooms. As precipitation intensity increases, the degree of algal blooms generally decreases. Thus, increased rainfall usually restricts the overall duration of algal blooms. However, in 2020, precipitation positively affected the CBD along the northeast Asian coast. This suggests that increased precipitation may enhance the nutrient load of estuaries, creating favorable hydrological conditions for phytoplankton growth, thereby increasing the likelihood of blooms in continental coastal zones[12].

[1] Gobler, C. J. *et al.*, Ocean warming since 1982 has expanded the niche of toxic algal blooms in the North Atlantic and North Pacific oceans. *Proceedings of the National Academy of Sciences* **114** 4975-4980 (2017).

[2] Hunter-Cevera, K. R. *et al.*, Physiological and ecological drivers of early spring blooms of a coastal phytoplankter. *SCIENCE* **354** 326-329 (2016).

[3] Beaugrand, G. & Kirby, R. R., How do marine pelagic species respond to climate change? Theories and observations. *ANNU REV MAR SCI* **10** 169-197 (2018).

[4] Doney, S. C., Fabry, V. J., Feely, R. A. & Kleypas, J. A., Ocean acidification: the other CO2 problem. *ANNU REV MAR SCI* **1** 169-192 (2009).

[5] Allen, J. T. *et al.*, Diatom carbon export enhanced by silicate upwelling in the northeast Atlantic. *NATURE* **437** 728-732 (2005).

[6] Kuttippurath, J., Sunanda, N., Martin, M. V. & Chakraborty, K., Tropical storms trigger phytoplankton blooms in the deserts of north Indian Ocean. *NPJ Climate and Atmospheric Science* **4** 11 (2021).

[7] Tang, W. *et al.*, Widespread phytoplankton blooms triggered by 2019–2020 Australian wildfires. *NATURE* **597** 370-375 (2021).

[8] Shi, X. *et al.*, Salinity decline promotes growth and harmful blooms of a toxic alga by diverting carbon flow. *GLOBAL CHANGE BIOL* **30** e17348 (2024).

[9] Luijendijk, E., Gleeson, T. & Moosdorf, N., Fresh groundwater discharge insignificant for the world's oceans but important for coastal ecosystems. *NAT COMMUN* **11** 1260 (2020).

[10] Pade, N. *et al.*, Trimethylated homoserine functions as the major compatible solute in the globally significant oceanic cyanobacterium Trichodesmium. *Proceedings of the National Academy of Sciences*

113 13191-13196 (2016).

[11] Ajani, P. A. *et al.*, Response of planktonic microbial assemblages to disturbance in an urban sub-tropical estuary. *WATER RES* **243** 120371 (2023).

[12] Wells, M. L. *et al.*, Harmful algal blooms and climate change: Learning from the past and present to forecast the future. *HARMFUL ALGAE* **49** 68-93 (2015).